Available online at www.sciencedirect.com
SCIENCE DIRECT®
ELSEVIER
Earth and Planetary Science Letters 216 (2003) 725–740
EPSL
www.elsevier.com/locate/epsl

Shear-enhanced compaction during non-linear viscous creep of porous calcite–quartz aggregates

Xiaohui Xiao *, Brian Evans

Department of Earth, Atmospheric, and Planetary Sciences, Massachusetts Institute of Technology, Cambridge, MA 02139, USA

Received 5 May 2003; received in revised form 8 September 2003; accepted 15 September 2003

Abstract

In this paper, we extend the previous studies of semi-brittle flow of synthetic calcite–quartz aggregates to a range of temperatures and effective pressures where viscous creep occurs. Triaxial deformation experiments were performed on hot-pressed calcite–quartz aggregates containing 10, 20 and 30 wt% quartz at confining pressure of 300 MPa, pore pressures of 50–290 MPa, temperatures of 673–1073 K and strain rates of 3.0×10^{-5}/s, 8.3×10^{-5}/s and 3.0×10^{-4}/s. Starting porosity varied from 5 to 9%. We made axial and volumetric strain measurements during the mechanical tests. Pore volume change was measured by monitoring the volume of pore fluid that flows out of or into the specimen at constant pore pressure. Yield stress increased with decreasing porosity and showed a dependence on effective pressure. Thus, the yield stress versus effective pressure can be described as a yield surface with negative slope that expands with decreasing porosity and increasing strain hardening, gradually approaching the envelope of strength at 10% strain, which has a positive slope. Creep of porous rock can be modeled to first order as an isolated equivalent void in an incompressible nonlinear viscous matrix. An incremental method is used to calculate the stress–strain curve of the porous material under a constant external strain rate. The numerical simulations reproduce general trends of the deformation behavior of the porous rock, such as the yield stress decreasing with increasing effective pressure and significant strain hardening at high effective pressure. The drop of yield stress with increasing porosity is modeled well, and so is the volumetric strain rate, which increases with increasing porosity.

Keywords: compaction; porosity; creep; effective pressure; axial and volumetric strain

1. Introduction

Fluid infiltration and fluid–rock interactions significantly affect metamorphism and regional deformation (e.g. [1]). If elevated pore fluid pressures were maintained close to lithostatic level by the continuous influx of fluid from the 'ductile root' of the fault zone, the strength of faults would be profoundly affected [2]. Permeability and fluid flow could also be influenced by crack healing and sealing processes [3]. Evolution of pore pressure during non-elastic deformation influences and is influenced by the mode of any volume changes, e.g. dilation or compaction. Although dilational modes are often associated with brittle mechanisms of deformation, either de-

* Corresponding author. Tel.: +1-617-253-3391; Fax: +1-617-258-0620.
E-mail addresses: xhxiao@mit.edu (X. Xiao), brievans@mit.edu (B. Evans).

0012-821X/03/$ – see front matter © 2003 Elsevier B.V. All rights reserved.
doi:10.1016/S0012-821X(03)00536-3

formation mode can be accomplished by either brittle or creep mechanisms [4–7]. Owing to the intimate relation of porosity, pore fluids, and mechanical properties, it is important to understand the mechanical behavior of porous rocks over a wide range of temperatures, pressures, and effective pressures, spanning the transition from brittle to plastic flow.

Both the deformation mode and mechanism in semi-brittle flow regime are affected by initial porosity [6,8] as well as grain size and modal composition [9,10]. For geological materials, there are few experiments investigating the effect of second phase on semi-brittle flow. At room temperature, adding rigid quartz inclusions with incoherent matrix–particle interface increased the range of pressure over which the transition between localized brittle failure and crystal plastic flow occurred within calcite rocks [10]. Under circumstances where the matrix deforms via plasticity or viscous creep, microvoids near second phase particles may nucleate or enlarge either by decohesion of the particle–matrix interface or by particle fracture [11,12]. The mechanical behavior of the aggregate may be greatly influenced by such microvoids; their presence can, for example, lead to pressure sensitivity of plastic flow and ductile fracture. There have been numerous studies performed on the mechanics of void growth or collapse in materials where the matrix deforms by power law creep [13–19]. However, much less has been done on porous rocks [7].

In this paper, we extend previous studies of semi-brittle flow of porous calcite–quartz aggregates to a range of temperatures and effective pressures where viscous creep occurs. Forty triaxial deformation experiments were performed on hot-pressed calcite–quartz aggregates containing 10, 20 and 30 wt% quartz at confining pressures of 300 MPa, pore pressures of 50–290 MPa, temperatures of 673–1073 K and strain rates of 3.0×10^{-5}/s, 8.3×10^{-5}/s and 3.0×10^{-4}/s. We made axial and volumetric strain measurement during the mechanical tests, measured pore volume changes by monitoring the volume of pore fluid that flowed out of or into the specimen at constant pore pressure, and performed in situ measurements of volumetric strain, permeability and storativity using argon gas as pore fluid. Descriptions of the measurement of permeability and storativity are left to a future contribution.

2. Experiments

2.1. Starting material

The calcite–quartz aggregates were fabricated from mixtures of powders of reagent grade $CaCO_3$ and crushed quartz in a commercial hot isostatic press (HIP) at 700°C and 200 MPa at Bodycote IMT, Andover, MA, USA. The mean grain size of both calcite and quartz particles is about 10 μm. Three large blocks, containing 10, 20, and 30% quartz, were HIPed. Cylindrical samples 10 mm diameter and 20 mm length were then cored from these blocks.

The bulk density was determined from the sample dimensions and weight. The porosity of the starting samples could then be calculated using the bulk density of the aggregate and the single crystal density of calcite and quartz. Starting porosities vary from 5 to 9%, higher porosity being correlated with higher quartz content (Table 1). From the scanning electron microscopy (SEM) micrographs (Fig. 1), two kinds of pores can be found: cracks along interfaces and spherical voids within the calcite matrix. Porosity was also estimated from the SEM micrographs using the image analysis program NIH image. Trace amounts of wollastonite (i.e. $<0.1\%$) are also present.

2.2. Procedure for experiments

The tests were carried out in a gas medium deformation apparatus (Paterson Instruments)

Table 1
Porosity of the starting material

Quartz content (wt%)	Porosity[a] (%)	Porosity[b] (%)
10	5.23 ± 0.56	3.35 ± 0.25
20	6.81 ± 0.62	4.93 ± 0.47
30	9.00 ± 0.18	7.27 ± 0.54

[a] Calculated based on sample dimension.
[b] Estimated from image analysis.

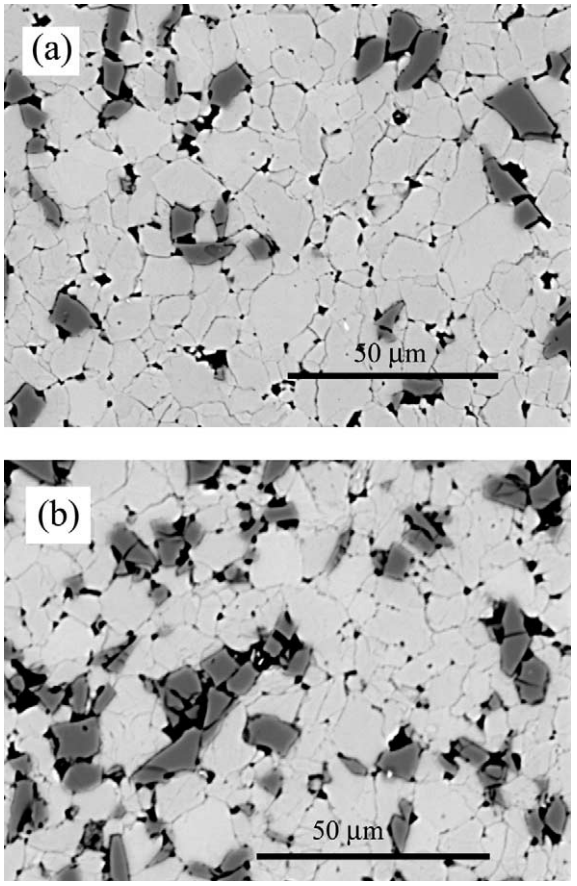

Fig. 1. Backscattered SEM image of hot-pressed two-phase aggregates with 10 wt% (a) and 20 wt% (b) quartz particles (dark gray). Two kinds of pores can be found: cracks along grain and interphase boundaries and spherical voids within the calcite matrix.

with internal furnace, internal load cell and a servo-controlled pore fluid volumometer. Specimens, split alumina spacers and alumina pistons were inserted in iron jackets. An inner copper shell was placed between the specimen and the iron jacket in order to provide more intimate contact around the cylindrical surface of the specimen and reduce the apparent pore volume associated with surface irregularities. The pore fluid pressure was monitored by a strain gauge pressure transducer with a resolution of 0.01 MPa. A servo-controlled motor drove the volumometer piston and maintained the pore pressure constant. The volume changes were then calculated from piston displacement recorded by a transducer (LVDT) attached to the end of the piston. The resolution of the LVDT is 0.3 μm.

Most tests consisted of two steps. The first involved applying confining and pore fluid pressures that were nearly equal, achieving the correct temperature, stabilizing the conditions; and then adjusting the pore pressure to its final value. This step is essentially an additional brief HIP treatment. The second step usually followed immediately after the first and was the deformation portion of the test, during which an axial load was applied.

2.2.1. HIP step

To begin the experiment, a confining pressure (about 230 MPa) was first applied, and the pore pressure increased to about 220 MPa. Argon gas was used as both the pore fluid and confining pressure medium. The specimen was heated at a rate of 15 K/min to 873 K, when the confining

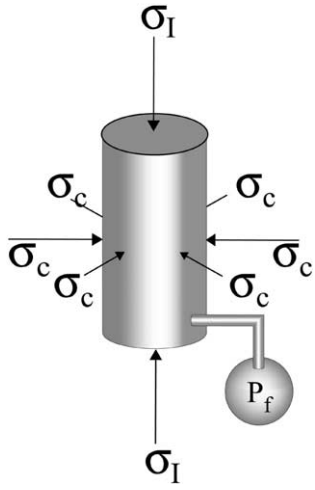

Fig. 2. Schematic drawing of the loading conditions for the porous samples. If the axial stress (σ_I) and the confining pressure (σ_c) are equal, the sample is said to be loaded in hydrostatic compression. Although here the term 'lithostatic' is more appropriate, in the sense of gravitational loading at the depth of burial, we follow the common practice of using 'hydrostatic' to refer to the pressure in the medium surrounding the specimen. When the hydrostatic pressure is larger than the pore fluid pressure, the sample will compact isometrically as occurs during HIP. When the axial stress is different than the confining pressure, the rock is said to be in conventional triaxial loading.

Table 2
Hydrostatic compaction of calcite–quartz aggregates

Run No.	Temperature (K)	Pore pressure (MPa)	Volumetric strain rate[a] (s^{-1})	Volumetric strain rate[b] (s^{-1})	Porosity[c] (%)	Load (kN)
10 wt% quartz						
10g09	873	200	–	8.29E-06	6.10	–
	873	150	3.40E-07	1.33E-06	6.08	1.3
	873	100	6.84E-07	1.63E-06	6.06	1.3
	873	50	3.67E-07	–	5.99	1.3
					5.89	
10g10	873	290	3.06E-07	5.82E-07	5.55	0.98
	873	250	2.32E-07		5.52	0.98
	873	200	3.27E-07	7.65E-07	5.47	0.98
	873	150	2.94E-07	2.94E-06	5.39	1.2
	873	100	3.89E-07	9.13E-07	5.26	1.2
	873	50	5.76E-07	1.79E-06	5.03	1.2
					4.94	
10g11	873	290	1.90E-07	2.05E-06	5.51	1.07
	973	290	5.10E-07	1.93E-06	5.47	1.07
	973	250	4.25E-07	1.80E-06	5.28	1.07
	973	200	7.01E-07	3.15E-06	5.11	1.07
	973	150	1.35E-06	2.16E-06	4.86	1.07
	973	100	3.73E-06	2.93E-06	4.69	1.07
	973	150	8.97E-07	1.36E-06	4.39	1.07
	973	100	1.21E-06	4.49E-06	4.39	1.07
	973	50	1.47E-06	9.18E-06	4.09	1.07
					3.86	
10g16	873	150	2.81E-07	6.85E-07	5.00	0.455
	873	100	3.68E-07	1.27E-06	4.93	0.455
	873	50	6.85E-07	1.29E-06	4.85	0.455
	873	50	3.62E-07	1.87E-06	4.74	0.32
	973	100	7.05E-07	1.12E-06	4.63	0.32
	973	50	1.25E-06	–	4.30	0.32
					4.12	
20 wt% quartz						
20g11	873	290	–	8.10E-08	5.93	–
	873	250	–	2.84E-07	5.90	–
	873	200	–	5.42E-07	5.86	–
	873	150	–	9.14E-07	5.71	–
					5.50	
20g14	873	200	4.81E-07	2.13E-06	6.00	1.12
	873	150	4.46E-07	3.35E-06	5.92	1.12
	873	100	6.11E-07	5.02E-06	5.81	1.12
	873	50	6.85E-07	6.80E-06	5.66	1.12
					5.34	
20g15	873	290	3.30E-07	2.34E-07	6.80	1.15
	1073	290	2.42E-06	2.35E-06	6.78	1.15
	1073	250	3.05E-06	2.48E-06	6.60	1.15
	1073	200	5.10E-06	5.27E-06	6.25	1.15
	1073	150	7.13E-06	7.56E-06	5.74	1.15
					4.82	
20g16	873	290	1.92E-07	–	7.00	1.07
20g19	873	250	2.78E-07	5.27E-07	7.70	0.38
	873	200	2.02E-07	6.78E-07	7.64	0.38
	873	150	7.67E-07	1.49E-06	7.57	0.38
	873	100	7.15E-07	1.17E-06	7.43	0.38
	873	50	8.67E-07	3.07E-06	7.17	0.38
					6.72	

Table 2 (*Continued*).

Run No.	Temperature (K)	Pore pressure (MPa)	Volumetric strain rate[a] (s^{-1})	Volumetric strain rate[b] (s^{-1})	Porosity[c] (%)	Load (kN)
30 wt% quartz						
30g13	873	290	6.80E-07	9.04E-07	8.70	1.05
	873	250	5.29E-07	1.21E-06	8.63	1.05
	873	200	5.62E-07	1.72E-06	8.49	1.05
	873	150	8.25E-07	1.87E-06	8.31	1.05
	873	200	5.07E-07	7.88E-07	8.09	1.05
	873	150	4.88E-07	9.14E-07	8.09	1.05
	873	100	6.92E-07	2.20E-06	8.00	1.05
	873	50	6.79E-07	2.15E-06	7.68	1.05
	973	250	3.95E-07	1.06E-06	7.37	1.05
	973	200	9.02E-07	1.44E-06	7.25	1.05
	973	150	1.34E-06	2.16E-06	7.09	1.05
	973	100	2.48E-06	4.49E-06	6.84	1.05
	973	200	8.38E-07	3.90E-07	6.31	1.05
	973	150	7.19E-07	1.51E-06	6.12	1.05
	973	100	1.48E-06	2.35E-06	6.05	1.05
	973	50	2.12E-06	5.66E-06	5.85	1.05
	873	50	3.06E-06	1.20E-06	5.20	1.05
					5.00	
30g14	1073	290	1.01E-06	–	8.10	1.06
	1073	250	3.08E-06	–	8.00	1.06
	1073	200	6.28E-06	–	7.76	1.06
	1073	150	4.72E-06	–	7.34	1.06
	1073	100	6.77E-06	–	6.83	1.06
	1073	50	5.80E-06	–	5.94	1.06
					5.58	
30g18	873	50	1.11E-06	7.75E-06	8.00	1.00
					7.00	

[a] Estimated from change of sample length.
[b] From volumometer.
[c] Starting porosity at pore pressure or temperature steps.

and pore pressures were adjusted to 300 MPa and 290 MPa respectively. The system was then allowed to settle for about 1 h. Finally, temperature and pore pressures were changed to the required values. This protocol provided uniform starting conditions before deformation and allowed us to estimate the pore space change with greater certainty.

We measured the volumetric compaction rate and the porosity change, during both hydrostatic loading and conventional triaxial loading (Fig. 2), by tracking the volumometer displacement Δx at constant temperature and constant pore pressure. Assuming that the temperature gradient in the connecting passage remains constant during the experiment, the volume of gas transferred can be calculated by multiplying the volumometer displacement by a correction that allows for the temperature difference between the sample and ambient. The correction factor corresponds to the ratio of the molar volume of argon at high temperature and room temperature [20]. Note that the porosity change obtained by the pore fluid method is the change in the connected pore space. In some experiments the total porosity change was estimated from the change in length of the specimen, assuming the compaction to be isotropic. The change in specimen length was measured by applying a small load of 0.5 kN (about 6 MPa, less than 10% of the specimen strength) to ensure the piston contacts the specimen, and noting the axial displacement reading. Some tests were run to determine the compaction rate under hydrostatic loading; for these experiments, pore pressure

steps were applied before subsequent loading under conventional triaxial loading.

An accurate independent measurement of the porosity when temperature and pressure have been reached is difficult, owing to thermal expansion and elastic compression of the sample and column pieces during heating and pumping. Efforts were made to maintain low effective pressure (about 10 MPa) when the specimen was being heated to the required temperature. The volumometer data show very little further compaction, indicating that the porosity change during this initial stage is relatively small. Therefore it is assumed that after the initialization procedure the porosity was the same as the initial porosity at room temperature and pressure. The porosity prior to the deformation can be obtained based on the subsequent volumometer displacement and the change of specimen length after the pore pressure was brought to the required value.

2.2.2. Deformation tests

Constant strain rate tests were performed at confining pressure of 300 MPa, pore pressures of 50–290 MPa, temperatures of 673–1073 K and strain rates of 3.0×10^{-5}/s, 8.3×10^{-5}/s and 3.0×10^{-4}/s. Volumetric strain was measured during the deformation tests.

2.3. Microstructure observation

All deformed samples were sectioned longitudinally for microstructural investigation. The sample surfaces were polished to 1 mm with Al_2O_3 powder and then treated by two-step chemo-mechanical etching with colloidal silica and deionized water. The etched samples were carbon-coated and digital images were captured in electron backscatter mode in a JEOL JXA-733 Superprobe. Grain size and porosity were estimated from the SEM micrographs using the image analysis program NIH image [21]. The grain boundaries, quartz phases or pores can be segmented manually by the density slice function in the image analysis program. After that, the image was changed to a binary file, from which the average grain size and porosity were measured.

3. Results

3.1. Hydrostatic compaction

As the solid framework of the calcite aggregate is loaded by the confining pressure, the porous rock will compact, provided that the fluid pressure (P_p) is less than the confining pressure (P_c), or in other words, if the effective pressure ($P_{eff} = P_c - P_p$) is positive. The hydrostatic compaction data and the microstructural analysis in-

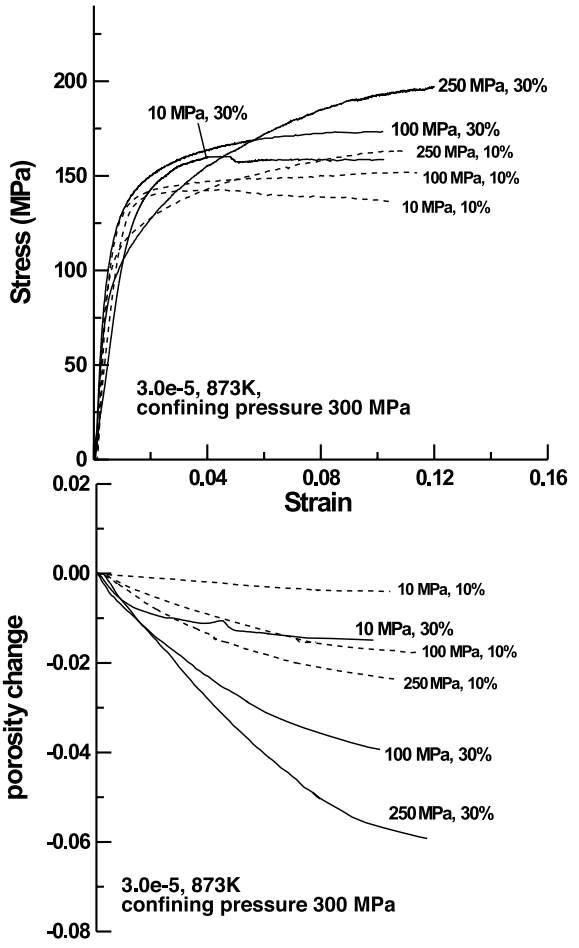

Fig. 3. Mechanical data for calcite–quartz aggregates with 10 and 30 wt% quartz at a temperature of 873 K, strain rate of 3.0×10^{-5}/s and confining pressure of 300 MPa. Differential stress and porosity changes are plotted against axial strain. Effective pressures are indicated. The solid curves are for 30 wt% quartz samples, and the dashed curves are for 10 wt% samples.

dicated that the samples have porosities of 4–7% after HIP, but before deformation, at temperatures up to 973 K. Thus, unless the effective pressure was larger than 10 MPa, which was the P_{eff} typical of the initial protocol, the densification rates were too small to be measured. In some experiments designed to measure the compaction rate under hydrostatic loading, pore pressure steps were applied before deformation to increase P_{eff}. Table 2 lists a set of data of porosity reduction rates at different effective pressures and temperatures. The hydrostatic compaction rates increase with increasing P_{eff}. Higher compaction rates were generally observed in the samples containing more quartz, probably owing to the increased initial porosity in those samples.

By analogy to the yield stress in the conventional deformation test, we can estimate a 'compaction yield pressure' for hydrostatic loading. Such a yield pressure would be the effective pressure at which the non-recoverable compaction was a substantial portion (say, 10%) of the total compaction and, under these conditions, would be rate-dependent. Therefore, for a volumetric strain rate ($\dot{\varepsilon}_v$) of 9.0×10^{-5}/s which is comparable with an axial strain rate ($\dot{\varepsilon}_a$) of 3.0×10^{-5}/s ($\dot{\varepsilon}_a = 1/3\dot{\varepsilon}_v$), the sample will yield at the effective pressure where the non-recoverable volumetric strain rate is about 9.0×10^{-6}/s. By extrapolating the hydrostatic compaction data (Table 2) to high effective pressure, we find that the yield pressure is around 350–400 MPa.

3.2. Yield stress, flow strength and porosity change

The two graphs in Fig. 3 show differential stress and porosity change versus axial strain, respectively, for the 10% and 30% quartz samples at effective pressure of 10, 100 and 250 MPa, temperature of 873 K and strain rate of 3×10^{-5}/s. Both the yield stress (elasticity limit, which is defined as the stress level for the onset of deviation from linearity) and flow strength at 10% axial strain are pressure-sensitive up to 1073 K, but yield stress is inversely related, while the strength at 10% strain is directly related (see Fig. 4). With increasing effective pressure, the stress–strain curves change from slight strain weakening at low effective pressure to continual strain hardening at high effective pressure. Owing to the strong

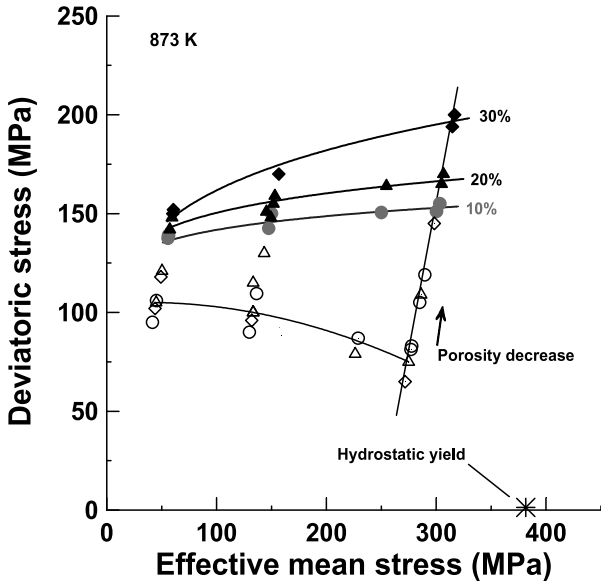

Fig. 4. Yield stress (open symbols) and flow strength (solid symbols) are plotted against effective mean stress. The flow strengths indicated are those at the point of 10% axial strain. The yield stress can be described by a yield surface with negative slope that expands with decreasing porosity and strain hardening, gradually approaching the flow strength envelope with positive slope.

Table 3
Mechanical data

Sample No.	Temperature (K)	Pore pressure (MPa)	Starting porosity (%)	Strain rate (s^{-1})	Yield stress (MPa)	Strength (MPa)	Porosity change (%)	Young's modulus (GPa)
10 wt% quartz								
CQ10g10	873	50	4.9	3.0×10^{-5}	83	152	−1.16	36.502
CQ10g11	873	50	3.9	3.0×10^{-5}	105	150	−0.44	30.239
	773	50	3.4	8.3×10^{-5}	175	230	−0.10	70.241
CQ10g12	673	290	5.2	8.3×10^{-5}	175	271	1.53	28.115
CQ10g13	873	200	4.3	3.0×10^{-5}	90	142.5	−1.98	27.298
CQ10g14	873	290	5.0	3.0×10^{-5}	95	137.5	−0.01	15.744
CQ10g15	673	290	5.5	8.3×10^{-5}	170	266	0.49	22.424
	673	50	6.0	8.3×10^{-5}	198	287	−1.64	39.16
CQ10g16	673	50	4.1	8.3×10^{-5}	186	300	−0.30	29.864
20 wt% quartz								
CQ10g08	873	205	6.1	3.0×10^{-5}	115	151	−0.88	39.736
	873	105	5.2	3.0×10^{-5}	130	172	−0.56	45.475
	873	55	4.6	3.0×10^{-5}	178	201	−0.24	73.987
CQ20g10	873	200	7.1	3.0×10^{-5}	79.5	148	−1.77	22.286
	873	200	5.3	3.0×10^{-5}	130	155	−0.98	32.941
	873	100	4.3	3.0×10^{-5}	134	170	–	36.979
	973	200	–	3.0×10^{-5}	110	126	–	13.923
	973	100	–	3.0×10^{-5}	120	130	–	10.505
CQ20g11	873	290	5.5	3.0×10^{-5}	122	150	−0.31	23.878
	873	250	5.2	3.0×10^{-5}	128	159	−0.50	38.081
	773	250	4.7	8.3×10^{-5}	186	238	−0.19	67.782
	773	250	4.5	3.0×10^{-5}	232	210	–	44.556
CQ20g12	773	290	6.8	3.0×10^{-5}	133	220	−0.64	31.035
	773	200	6.2	3.0×10^{-5}	164	243	−1.41	51.338
	773	200	4.8	8.3×10^{-5}	218	260	−0.56	133.601
	773	100	4.2	8.3×10^{-5}	212	273	−0.91	45.969
CQ20g13	773	100	6.6	3.0×10^{-5}	93	250	−2.61	25.166
	773	100	4.0	8.3×10^{-5}	208	245	−0.72	93.03
CQ20g16	673	290	7.0	3.0×10^{-5}	135	260	0.09	36.352
	673	290	7.1	8.3×10^{-5}	255	265	0.64	82.723
	673	290	7.7	3.0×10^{-5}	276	297	0.54	166.615
CQ20g17	673	50	6.5	8.3×10^{-5}	140	310	−3.19	43.24
CQ20g18	873	290	7.1	3.0×10^{-5}	102	144	–	17.644
CQ20g19	673	50	6.7	8.3×10^{-5}	178	351	−0.09	37.221
CQ20g20	873	200	5.6	3.0×10^{-5}	75	130	−0.88	22.091
	873	200	4.7	8.3×10^{-5}	130	168	−0.70	38.502
	873	200	4.0	3.0×10^{-4}	150	189	−0.44	49.94
CQ20g21	673	200	5.9	3.0×10^{-5}	100	272	−0.96	28.975
	673	200	4.9	8.3×10^{-5}	262	310	−0.33	52.951
	673	200	4.6	3.0×10^{-4}	300	325	0.00	77.678
30 wt% quartz								
CQ30g09	1073	150	7.5	8.3×10^{-5}	47	90	–	16.929
	1073	75	–	8.3×10^{-5}	70	110	–	20.838
	1073	0	–	8.3×10^{-5}	82	116	–	22.505
CQ30g10	873	210	8.6	3.0×10^{-5}	72	170	−0.56	31.501
	873	210	8.0	3.0×10^{-5}	124	176	−0.60	41.394
	873	105	7.4	3.0×10^{-5}	102	180	–	48.429
	873	105	–	3.0×10^{-5}	132	200	–	
CQ30g11	873	200	8.5	3.0×10^{-5}	108	175	−1.19	27.135
	873	150	7.3	3.0×10^{-5}	119	183	−0.89	34.477
	873	50	6.4	3.0×10^{-5}	125	195	−0.90	37.951
	773	50	5.5	3.0×10^{-5}	180	275	–	71.024
	773	50	–	8.3×10^{-5}	252	278	–	80.514

Table 3 (*Continued*).

Sample No.	Temperature (K)	Pore pressure (MPa)	Starting porosity (%)	Strain rate (s^{-1})	Yield stress (MPa)	Strength (MPa)	Porosity change (%)	Young's modulus (GPa)
CQ30g12	1073	290	8.6	8.3×10^{-5}	60	80	−0.92	12.541
	1073	200	7.7	8.3×10^{-5}	58	95	−1.87	19.538
	773	200	5.8	8.3×10^{-5}	125	250	−0.20	45.308
CQ30g13	873	50	5.0	3.0×10^{-5}	112	212	−2.11	33.931
CQ30g14	873	285	8.5	3.0×10^{-5}	100	160	−1.37	11.084
	873	50	5.6	8.3×10^{-5}	133	241	−1.97	45.53
CQ30g15	773	290	8.5	3.0×10^{-5}	150	213	−1.28	41.00
	773	290	7.2	8.3×10^{-5}	–	210	0.40	–
	773	290	7.6	3.0×10^{-4}	210	218	0.91	44.539
CQ30g16	673	290	8.8	8.3×10^{-5}	105	300	1.69	38.99
	673	150	10.5	8.3×10^{-5}	245	350	−2.16	63.369
CQ30g18	873	50	7.0	3.0×10^{-5}	78	195	–	21.134
CQ30g19	873	200	8.6	8.3×10^{-5}	75	170	−2.30	20.112
	873	200	6.3	3.0×10^{-4}	168	190	−0.70	40.155
CQ30g20	873	290	8.8	3.0×10^{-5}	65	128	−0.75	14.253
	873	290	8.1	8.3×10^{-5}	110	140	0	23.535
	873	290	8.1	3.0×10^{-4}	135	142	0.78	25.577
CQ30g23	673	200	8.9	3.0×10^{-5}	88	263	−1.20	21.123
	673	200	7.7	8.3×10^{-5}	252	299	−0.62	40.423
	673	200	7.1	3.0×10^{-4}	290	290	0.04	49.313

strain hardening at high effective pressure, steady states are not reached, at least up to 20% axial strain. The crossover of strength at different confining pressures with increasing strain has been observed previously in lithographic limestone (probably Solnhofen) [4]. A compilation of the mechanical data from the current paper is given in Table 3.

Fig. 5 shows the stress–strain curves of the 20 wt% quartz samples deformed at an effective pres-

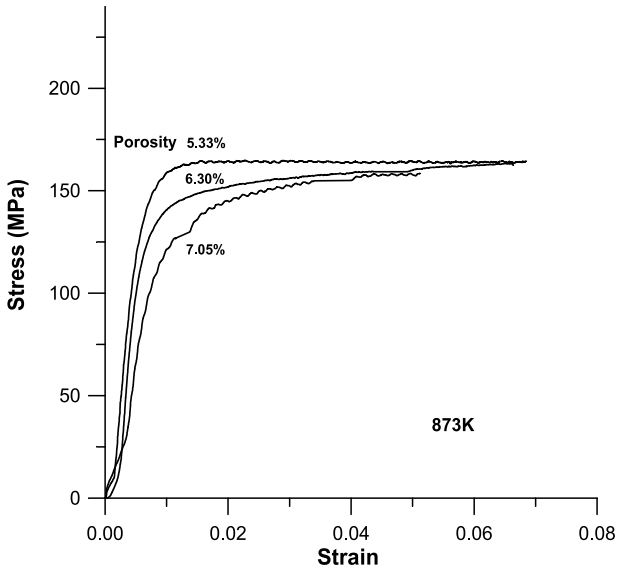

Fig. 5. Stress–strain curves of 20% quartz samples with different initial porosity. Deformation took place at 873 K, effective pressure of 100 MPa, and a strain rate of 8.3×10^{-5}/s. Note that yield stress increases with decreasing porosity.

sure of 100 MPa, but with different starting porosities. Clearly, yield stress increases with decreasing porosity. Thus, the yield stress versus effective pressure can be described as a yield surface with negative slope that expands with decreasing porosity and increasing strain hardening, gradually approaching the envelope of strength at 10% strain, which has a positive slope (Fig. 4).

In general, the mechanical data show that strength of two-phase aggregates at 10% strain increases with increasing quartz content (Fig. 6), in agreement with earlier studies [22–24]. Because the strengthening at high effective pressure is larger than that under low effective pressure, the strength difference between the samples containing 10% and 30% quartz is about 50 MPa at an effective pressure of 250 MPa (pore pressure of 50 MPa) and at 873 K, but the difference between those two aggregates is less than 10 MPa at an effective pressure of 10 MPa (Fig. 6).

During deformation at elevated temperature and effective pressure, there is an accelerated compaction in comparison to the initial HIP step. (As mentioned above, much of the initial porosity remains after application of the confining pressure and pore pressure.) This shear-enhanced compaction indicates that deviatoric stresses provide significant inelastic contribution to the volumetric strain. Dilation occurred only at low temperature (673 K), high strain rate 8.3×10^{-5}/s and effective pressure of 10 MPa. SEM micrographs (Fig. 7) showed that samples deformed at high effective pressure had lower porosity than those deformed at low effective pressure, and that microcracks are rare in the deformed samples.

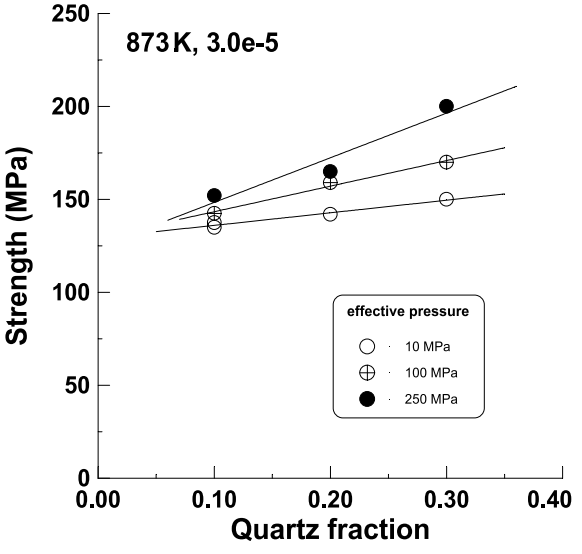

Fig. 6. Bulk strength versus quartz fraction of calcite–quartz aggregates at effective pressures of 10, 100 and 250 MPa. All experiments were done at 873 K, strain rate of 3.0×10^{-5}/s.

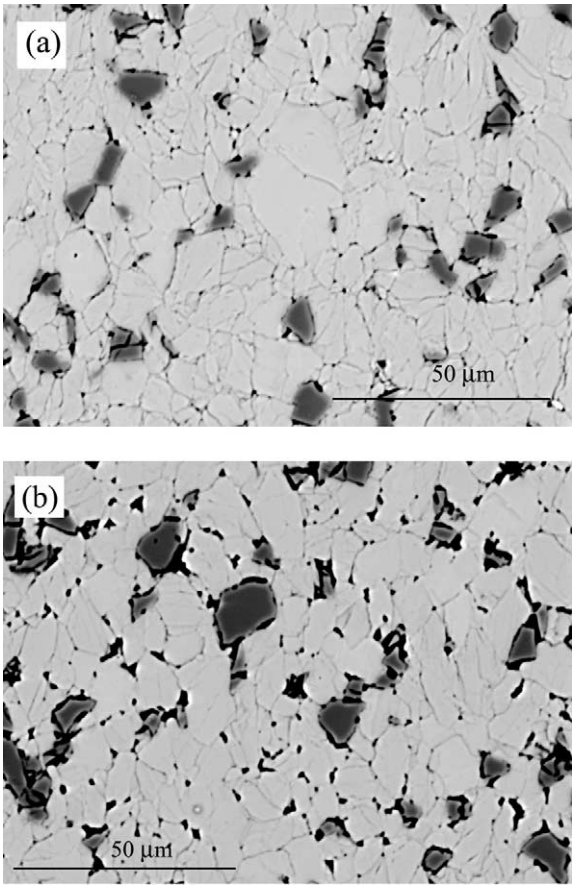

Fig. 7. Backscattered SEM image of deformed samples containing 10 wt% quartz. (a) Effective pressure: 250 MPa. (b) Effective pressure: 10 MPa. Clearly, the sample deformed at high effective pressure has lower porosity.

4. Discussion

4.1. General

Our mechanical data exhibit pressure-depen-

dent strength under conditions where the local deformation mechanisms are probably dominated by dislocation creep [25–27]. Here we distinguish between the term 'creep', i.e. rate-dependent processes, and 'plastic', i.e. rate-independent processes [28,29]. Traditionally, the yield cap model is applied to porous materials that deform via rate-independent mechanical processes including those occurring at room temperature in granular soil [30], clay [31], porous sandstone [6] and limestone [7]. Wong and co-workers have suggested that the two-yield surface (cap) model provides a constitutive framework for the analysis of the cataclastic flow in porous silicates at room temperature, where grain crushing and microcracking are the dominant micromechanical processes [6,32]. In Solnhofen limestone deformed at room temperature and pressures up to 435 MPa [7], compaction occurs by plastic flow, but, with increasing strain, deformation evolves to dilatant, cataclastic flow and ultimately shear localization. Granular flow and the two-yield surface may also be applied to the deformation of partially molten granite when the melt pressure is elevated [33].

We wish to draw an analogy between the experiments on porous calcite aggregates deforming by rate-dependent processes and previous descriptions using the two-yield surface model for rate-independent behavior. Thus, in the following, we discuss 'yield stresses' and 'yield surfaces' with the understanding that these parameters are broadened from their usual restriction to perfectly plastic behavior.

In our experiments, the yield stress of the porous aggregates can be described by a yield surface with negative slope in plots of differential stress versus pressure and a direct, probably non-linear, dependence on strain rate. At a given temperature and strain rate, as the material deforms and porosity decreases, flow strength increases. We infer that the yield surface expands and that the slope of the yield surface flattens, gradually becoming positive (Fig. 4). Observations of the microstructure in these experiments did not identify microcracks in most of these samples. Macroscopic measurements indicate compaction with increasing axial strain, but with no strain localization up to 20% axial strain. Ultimately, the strength of the aggregate probably approaches that for creep flow of a non-porous marble with constant volume, although more data at large strains are needed. Considering the broad variety of materials, the wide range of conditions, and the multiplicity of micromechanical mechanisms for which the yield cap model seems to be indicated, we infer by induction that this model will be generally applicable to the deformation of most porous materials, regardless of the mechanisms of deformation.

4.2. *Creep constitutive equation for porous material*

Initial research on the effects of voids on mechanical behavior of porous metals considered the axisymmetric deformation of a spherical void embedded in an infinite block of perfectly plastic material [13]. Budiansky et al. [15] generalized these earlier studies to include non-linearly viscous deformation of the matrix. Approximate constitutive relations for solids containing a dilute concentration of spherical voids were derived by Duva and Hutchinson [16]. Other studies have focused on the effect of void distributions [12,17] and the effect of void shape on the overall response of the material [18].

Following the success of Baud et al. [7] who used a model of plastic pore collapse [34] to analyze plastic behavior of limestone at room temperature, we employed the creep model [15] to analyze the high-temperature results. Assume that the creep compaction of porous rock can be modeled as a medium containing an isolated equivalent void. Although there is discussion regarding the best description of viscous creep in marbles, for simplicity, we assume that the matrix material is an incompressible, non-linearly viscous material. We adopt the sign convention that compression is positive. Then, under compression σ, the strain rate is given by the power law:

$$\dot{\varepsilon} = \dot{\varepsilon}_0(\sigma/\sigma_0)^n \quad (1)$$

where $\dot{\varepsilon}_0$ and σ_0 are reference values. Furthermore, the void is assumed to be axisymmetric with respect to the principal axes of the remote

Table 4
Duva and Hutchinson [16]

n	f^*	x^*	k
1	0.833	0	2.25
1.5	0.965	−0.019	2.42
2	1.05	−0.031	2.55
3	1.16	−0.045	2.71
5	1.26	−0.058	2.88
10	1.35	−0.070	3.06
∞	1.46	−0.083	3.30

stress (Σ) and the surface of the void to be traction-free.

The description of void growth or collapse requires an accurate solution for the velocity field surrounding the void, and hence, the dilatation or compaction rate of the void as a function of stress state and hardening exponent n. Budiansky et al. [15] generated approximate Rayleigh–Ritz solutions for a spherical void based on the minimum principle for velocities stated by Hill [35]. Approximate results are given for different loading conditions, as characterized by the stress triaxiality, x, defined as:

$$x = \Sigma_m \Sigma_e \tag{2}$$

where $\Sigma_m = 1/3\Sigma_{kk}$ is the remote mean stress and $\Sigma_e = (3/2 S_{ij} S_{ij})^{1/2}$ is the remote effective stress. S_{ij} is the deviator of Σ.

For high triaxiality ($|x| > 1$), the normalized dilation rate is given by:

$$\frac{\dot{V}}{\dot{E}V} = \frac{3}{2} m \left\{ \frac{3|x|}{2n} - G(n,m) \right\}^n \tag{3}$$

where V is void volume, $\dot{V}$ the rate of change of volume. $\dot{E}$ is the remote strain rate, $m = \mathrm{sign}(x)$, and:

$$-G(n,m) = (n-1)[n + g(m)]/n^2 \tag{4}$$

with $g(1) = 0.4319$ and $g(-1) = 0.4031$.

For low triaxiality ($|x| < 1$), the approximation derived by Duva and Hutchinson [16] based on the numerical results of Budiansky et al. [15] is:

$$\frac{\dot{V}}{\dot{E}V} = k(n)[x - x^*(n)] \tag{5}$$

Values of k and x^* are listed in Table 4.

The potential function for an isolated spherical void in an infinite block of power law material, together with the results of dilation rate given by Eqs. 3 and5, can then be used to arrive at an constitutive relation [16]. The creep rate derived for high triaxiality is approximately:

$$\dot{E}_{ij} = \frac{3}{2}\dot{\varepsilon}_0 \left(\frac{\Sigma_e}{\sigma_0}\right)^{n-1} \frac{S_{ij}}{\sigma_0} + \rho \dot{\varepsilon}_0 \left(\frac{\Sigma_e}{\sigma_0}\right)^n \left[\frac{3|x|}{2n} - G\right] \left[\frac{3}{2}(-nG)\frac{S_{ij}}{\Sigma_e} + \frac{1}{2}\mathrm{sign}(x)\delta_{ij}\right] \tag{6}$$

and for low triaxiality:

$$\dot{E}_{ij} = \frac{3}{2}\dot{\varepsilon}_0 \left(\frac{\Sigma_e}{\sigma_0}\right)^{n-1} \frac{S_{ij}}{\sigma_0} + \rho \dot{\varepsilon}_0 \left(\frac{\Sigma_e}{\sigma_0}\right)^n \left\{\frac{3}{2}[(n+1)f^* + \frac{1}{2}k(n-1)x^2]\frac{S_{ij}}{\Sigma_e} + \frac{1}{3}kx\delta_{ij}\right\} \tag{7}$$

where Σ_e is the effective stress and S_{ij} is the stress deviator, ρ is the porosity, δ_{ij} is the Kronecker delta. Values of f^* are listed in Table 4.

4.3. Comparison with experimental data

In Fig. 8, the experimental data for creep com-

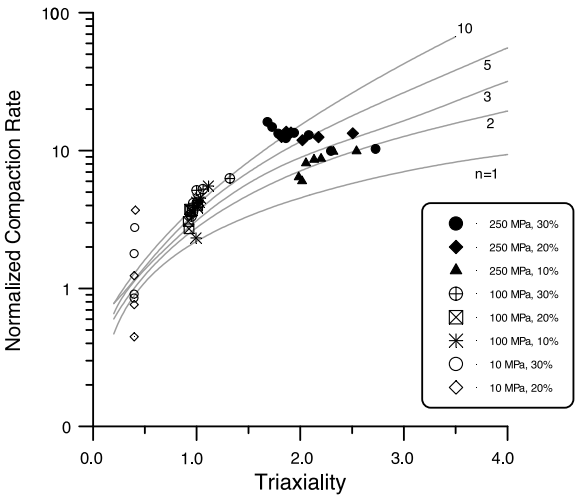

Fig. 8. Comparison of the experimental data to the theoretical model of void growth or collapse in a power law viscous matrix material [15]. The normalized compaction rate is the ratio of the volumetric and shear strain rates. The triaxiality measure is the ratio of the average mean stress to the magnitude of the deviatoric stress, i.e. higher mean stresses plot to the right of the graph.

paction of synthetic marble are compared to the theoretical model. The plot shows actual and predicted values of the normalized void compaction rate, as measured by $\dot{V}/(\dot{E}V)$, as a function of triaxiality (the ratio of mean effective stress to the deviatoric stress). The solid lines are the approximate results from Eqs. 3 and 4. The symbols represent the experiment data of calcite–quartz aggregates at effective pressures of 10, 100 and 250 MPa. Agreement of the two is good at high effective pressure (100 and 250 MPa) but not as good at low effective pressure; it is possible that brittle mechanisms become more important with decreasing effective pressure.

4.4. Modeling deformation behavior of porous material

It is obvious that the deformation behavior of a porous material will be strain history-dependent, because porosity and pore shape will change during deformation. An incremental method adopted from Murali and Weng [36] was used to calculate the stress–strain curve of the porous material under a constant external strain rate. The total strain rate is the sum of the elastic and creep strain rate. Therefore, over a short time dt, the elastic strain can be calculated from:

$$d\varepsilon^e = d\varepsilon - d\varepsilon^c \quad (8)$$

where $d\varepsilon^e$ and $d\varepsilon^c$ are the elastic and creep strain increments, respectively. The total strain $d\varepsilon = \dot{\varepsilon} \cdot dt$, where $\dot{\varepsilon}$ is the constant strain rate. The creep strain $d\varepsilon^c$ can be calculated from Eqs. 6 and 7. The macroscopic stress increment $d\sigma$ can be calculated from:

$$d\sigma = E \cdot d\varepsilon^e \quad (9)$$

where E is the elastic modulus. At the end of each time increment, the strain rate of the voids given by Eqs. 3 and 5 is used to update the porosity. Together with the new porosity, the macroscopic stress ($\sigma + d\sigma$) provides the new creep rate from Eqs. 6 and 7 for the next time increment. This incremental procedure is repeated to obtain the entire stress–strain curve.

In this study, the pores are idealized as spherical and perfectly drained. The initial shape and evolution of pores probably has a substantial effect upon the behavior of the porous solid. However, given the complexity introduced by the quartz particles, we neglect the effect of pore shape in this approximation. We consider the samples containing 10% quartz, deformed at 873 K and confining pressure of 300 MPa. The following creep constants (Eq. 1), based on previous studies of calcite–quartz aggregates [22,23], were used: $\dot{\varepsilon} = 3 \times 10^{-5}$/s, $\sigma_0 = 165$ MPa; $n = 4$. The Young modulus E is 80 GPa [37].

Strain–stress curves of calcite–quartz aggregates (10% quartz) calculated for a constant strain rate of 3×10^{-5}/s and 873 K are shown in Fig. 8. The results are presented in terms of differential stress versus axial strain and volumetric strain (porosity change) versus axial strain. Fig. 9A shows the calculated curves at a starting porosity of 5% and effective pressure of 250, 100 and 10 MPa. The numerical simulations reproduce general trends of the deformation behavior of the calcite–quartz aggregates, including decreases in yield stress with increasing effective pressure and significant strain hardening at high effective pressure. The volumetric strain rate is markedly reduced at low effective pressure. Fig. 9B shows the results for the effective pressure of 100 MPa and starting porosity varying from 1.0% to 8.0%. The drop of yield stress with increasing porosity is modeled well, so is the volumetric strain rate, which increases with increasing porosity.

The modeling does not predict the experimental results quantitatively, however; perhaps because: (i) the simple flow law (Eq. 1) does not include strain hardening observed in dense aggregates during creep; or (ii) complexities may be introduced by the presence of the quartz particles. One may speculate that a more sophisticated flow law (other than Eq. 1), which also described the strengthening effect of second phases, would probably predict the results more accurately. A third possibility exists: (iii) local values of pore pressure might evolve. Some pores are isolated and some more may become unconnected during deformation. Then the local pore pressure will increase, as the pore size decreases, and the local effective pressure will not remain constant. And, a fourth reason may also be important: (iv) the

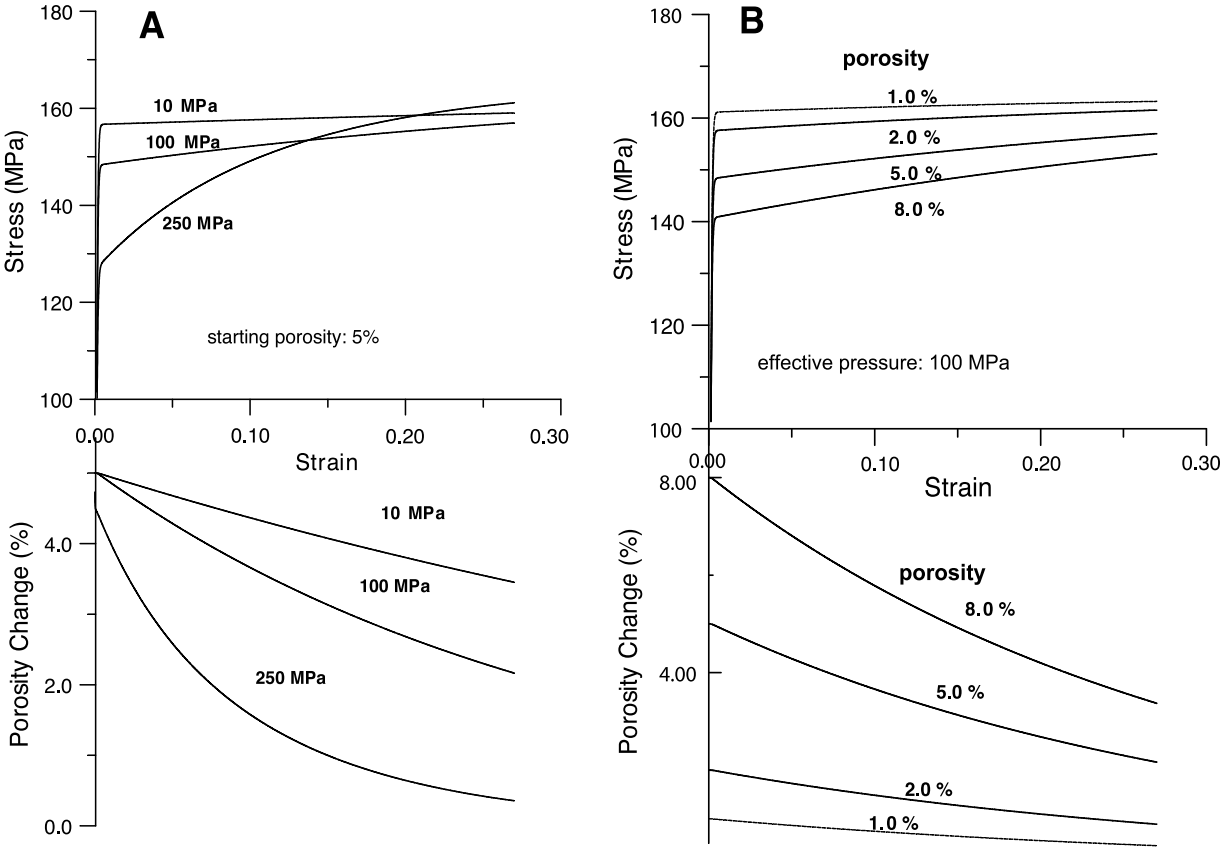

Fig. 9. Numerical simulation of the deformation behavior for the porous calcite–quartz aggregates under a constant strain rate of 3.0×10^{-5}/s, temperature of 873 K. (A) Calculated curves at a starting porosity of 5% and effective pressure of 250, 100 and 10 MPa. (B) Results for the effective pressure of 100 MPa and starting porosity varying from 1.0% to 8.0%. The numerical results are quite similar qualitatively to the experimental results.

actual stresses around the pores are not well approximated by those around a spherical pore.

5. Conclusions

In this study, our mechanical data of the porous calcite–quartz aggregates exhibit pressure-dependent strength under conditions where viscous creep occurs. The yield cap model seems to be applicable for the deformation of the porous aggregates. Yield stress can be described by a yield surface with negative slope in plots of differential stress versus pressure. At a given temperature and strain rate, as the material deforms and porosity decreases, flow strength increases. During deformation at elevated temperature and effective pressure, compaction rates are accelerated in comparison to those during hydrostatic compaction. This shear-enhanced compaction indicates that deviatoric stresses provide significant inelastic contribution to the volumetric strain. Dilation and strain localization are not observed in most of these samples, at least for axial strain $<20\%$. The experimental data of shear-enhanced compaction are in reasonable agreement with the creep model [15] assuming that the creep compaction of porous rock can be modeled as a medium containing an isolated equivalent void. Finally, an incremental method adopted from Murali and Weng [36] was used to calculate the strain–stress curve of the porous material under a constant external

strain rate. We find qualitative agreement between the experimental data and the numerical simulations.

Acknowledgements

We profited from fruitful discussions with J. Renner, G. Dresen and P. Baud. Supports from the Department of Energy through Grant DEFG02-00ER9903307, NSF EAR 0125669 are acknowledged. The manuscript benefited from the constructive reviews of T.-f. Wong and an anonymous reviewer. *[SK]*

References

[1] M.A. Etheridge, V.J. Wall, S.F. Cox, R.H. Vernon, High fluid pressures during regional metamorphism and deformation: Implication for mass transport and deformation mechanisms, J. Geophys. Res. 89 (1984) 4344–4358.

[2] J.R. Rice, Fault stress, pore pressure distribution, and the weakness of the San Andreas Fault, in: B. Evans, T.-f. Wong (Eds.), Fault Mechanics and Transport Properties of Rocks, Academic Press, New York, 1992, pp. 475–503.

[3] J. Walder, A. Nur, Porosity reduction and crustal pore pressure development, J. Geophys. Res. 89 (1984) 11539–11548.

[4] J.M. Edmond, M.S. Paterson, Volume changes during the deformation of rocks at high pressure, Int. J. Rock Mech. Miner. Sci. 9 (1992) 161–182.

[5] B. Evans, J.T. Fredrich, T.-F. Wong, The brittle–ductile transition in rocks; recent experimental and theoretical progress, in: A.G. Duba, W.B. Durham, J.W. Handin, H.F. Wang (Eds.), The Brittle–Ductile Transition in Rocks; Geophys. Monogr. 56 (1990) 1–20.

[6] T.-f. Wong, C. David, W. Zhu, The transition from brittle faulting to cataclastic flow in porous sandstones: Mechanical deformation, J. Geophys. Res. 102 (1997) 3009–3026.

[7] P. Baud, A. Schubnel, T. Wong, Dilatancy, compaction, and failure mode in Solnhofen limestone, J. Geophys. Res. B Solid Earth 105 (2000) 19289–19303.

[8] W. Zhu, T.-f. Wong, The transition from brittle faulting to cataclastic flow: Permeability evolution, J. Geophys. Res. 102 (1997) 3027–3041.

[9] J.T. Fredrich, B. Evans, T.-f. Wong, Micromechanics of the brittle to plastic transition in Carrara marble, J. Geophys. Res. Solid Earth Planets 94 (B4) (1989) 4129–4145.

[10] G. Dresen, B. Evans, Brittle and semibrittle deformation of synthetic marbles composed of two phases, J. Geophys. Res. 98 (B7) (1993) 11921–11933.

[11] S.H. Goods, L.M. Brown, The nucleation of cavities by plastic deformation, Acta Metall. 27 (1979) 1–15.

[12] J. Koplik, A. Needleman, Void growth and coalescence in porous plastic solids, Int. J. Solids Structures 24 (1988) 835–853.

[13] J.R. Rice, D.M. Tracey, On the ductile enlargement of voids in traxial stress fields, J. Mech. Phys. Solids 17 (1969) 201–217.

[14] A.L. Gurson, Continuum theory of ductile rupture by void nucleation and growth – Part I: Yield criteria and flow rules for ductile media, J. Eng. Mater. Technol. 99 (1977) 2–15.

[15] B. Budiansky, J.W. Hutchinson, S. Slutsky, Void growth and collapse in viscous solids, in: H.G. Hopkins, M.J. Sewell (Eds.), Mechanics of Solids, Pergamon Press, Oxford, 1982, pp. 13–45.

[16] J.M. Duva, J.W. Hutchinson, Constitutive potentials for dilutely voided nonlinear materials, Mech. Mater. 3 (1984) 41–54.

[17] V. Tvergaard, Numerical study of localization in a void-sheet, Int. J. Solids Structure 25 (1989) 1143–1156.

[18] B.J. Lee, M.E. Mear, Studies of the growth and collapse of voids in viscous solids, J. Eng. Mater. Technol. 116 (1994) 348–358.

[19] A. Needleman, V. Tvergaard, E. vanderGiessen, Evolution of void shape and size in creeping solids, Int. J. Damage Mech. 4 (1995) 134–152.

[20] R.B. Stewart, R.T. Jacobsen, Thermodynamic properties of argon from the triple point to 1200 K with pressure to 1000 MPa, J. Phys. Chem. Ref. Data 18 (1989) 639–798.

[21] M. Herwegh, A new technique to automatically quantify microstructures of fine grained carbonate mylonites: Two-step etching combined with SEM imaging and image analysis, J. Struct. Geol. 22 (2000) 391–400.

[22] G. Dresen, B. Evans, D.L. Olgaard, Effect of quartz inclusions on plastic flow in marble, Geophys. Res. Lett. 25 (1998) 1245–1248.

[23] G. Siddiqi, Transport Properties and Mechanical Behavior of Synthetic Calcite–Quartz Aggregates, Ph.D. Thesis, MIT, Cambridge, MA, 1997.

[24] A.N. Walker, E.H. Rutter, K.H. Brodie, Experimental study of grain-size sensitive flow of synthetic, hot-pressed calcite rocks, in: R.J. Knipe, E.H. Rutter (Eds.), Deformation Mechanisms, Rheology and Tectonics, Geol. Soc. London Spec. Publ. 54 (1990) 259–284.

[25] J.H.P. de Bresser, C.J. Spiers, Slip systems in calcite single crystals deformed at 300–800°C, J. Geophys. Res. 98 (1993) 6397–6409.

[26] E.H. Rutter, The influence of temperature, strain rate, and interstitial water in the experimental deformation of calcite rocks, Tectonophysics 43 (1984) 311–334.

[27] J. Renner, B. Evans, Do calcite rocks obey the power law creep equation?, in: G. Pennock (Ed.), Deformation Mechanisms, Rheology, and Tectonics, Current Status and Future Perspectives, Geol. Soc. London Spec. Vol. 200 (2002) 309–329.

[28] M.F. Ashby, R.A. Verall, Micromechanisms of flow and

fracture, and their relevance to the rheology of the upper mantle, Phil. Trans. R. Soc. London 288 (1978) 59–95.
[29] J.M. Branlud, K. Regenauer-Lieb, D.A. Yuen, Weak zone formation for initiating subduction from thermo-mechanical feedback of low-temperature plasticity, Earth Planet. Sci. Lett. 190 (2001) 237–250.
[30] F.L. DiMaggio, I.S. Sandler, Material model for granular soils, J. Eng. Mech. Div. Am. Soc. Civ. Eng. 97 (1971) 935–950.
[31] T. Hueckel, A. Peano, R. Pellegrini, A constitutive law for thermo-plastic behaviour of rocks: an analogy with clays, Surv. Geophys. 15 (1994) 643–671.
[32] J. Zhang, T.-f. Wong, D.M. Davis, Micromechanics of pressure-induced grain crushing in porous rocks, J. Geophys. Res. 95 (1990) 341–352.
[33] E.H. Rutter, D.H.K. Neumann, Experimental deformation of partially molten Westerly granite under fluid-absent conditions, with implications for the extraction of granitic magmas, J. Geophys. Res. 100 (1995) 15697–15715.
[34] J.H. Curran, M.M. Carroll, Shear stress enhancement of void compaction, J. Geophys. Res. 84 (B3) (1979) 1105–1112.
[35] R. Hill, New horizons in the mechanics of solids, J. Mech. Phys. Solids 5 (1956) 66–74.
[36] K. Murali, G.J. Weng, Theoretical calculation of anisotropic creep and stress–strain behavior for a class of metal–matrix composites, Metall. Trans. A 24A (1992) 2049–2059.
[37] G. Simmons, H. Wang, Single Crystal Elastic Constants and Calculated Aggregate Properties: A Handbook, MIT Press, Cambridge, MA, 1971.